

Investigating and Improving Latent Density Segmentation Models for Aleatoric Uncertainty Quantification in Medical Imaging

M. M. Amaan Valiuddin, Christiaan G. A. Viviers, Ruud J. G. van Sloun, *Member, IEEE*, Peter H. N. de With, *Fellow, IEEE*, and Fons van der Sommen, *Member, IEEE*

Abstract—Data uncertainties, such as sensor noise, occlusions or limitations in the acquisition method can introduce irreducible ambiguities in images, which result in varying, yet plausible, semantic hypotheses. In Machine Learning, this ambiguity is commonly referred to as aleatoric uncertainty. In image segmentation, latent density models can be utilized to address this problem. The most popular approach is the Probabilistic U-Net (PU-Net), which uses latent Normal densities to optimize the conditional data log-likelihood Evidence Lower Bound. In this work, we demonstrate that the PU-Net latent space is severely sparse and heavily under-utilized. To address this, we introduce mutual information maximization and entropy-regularized Sinkhorn Divergence in the latent space to promote homogeneity across all latent dimensions, effectively improving gradient-descent updates and latent space informativeness. Our results show that by applying this on public datasets of various clinical segmentation problems, our proposed methodology receives up to 11% performance gains compared against preceding latent variable models for probabilistic segmentation on the Hungarian-Matched Intersection over Union. The results indicate that encouraging a homogeneous latent space significantly improves latent density modeling for medical image segmentation.

Index Terms—Probabilistic Segmentation, Aleatoric Uncertainty, Latent Density Modeling

I. INTRODUCTION

Supervised deep learning segmentation algorithms rely on the assumption that the provided reference annotations for training reflect the unequivocal ground truth. Yet, in many cases, the labeling process contains substantial inconsistencies in annotations by domain-level experts. These variations manifest from inherent ambiguity in the data (e.g., due to occlusions, sensor noise, etc.), also referred to as the *aleatoric uncertainty* [1]. In turn, subjective interpretation of readers leads to multiple plausible annotations. This phenomena is generally expressed with multi-annotated data, revealing that labels may vary within and/or across annotators (also known as the *intra-/inter-observer variability*). While this concept is generic, the most significant impact of this phenomenon can be encountered in medical image segmentation (see Figure 1), where poorly guided decision-making by medical experts can have direct adverse consequences on patients [2]–[11]. Given

M.M.A. Valiuddin, C.G.A. Viviers, R.J.G. van Sloun, P.H.N. de With and F. van der Sommen are with the Department of Electrical Engineering at the Eindhoven University of Technology, Eindhoven, 5612 AZ, The Netherlands (corresponding author e-mail: m.m.a.valiuddin@tue.nl).

R.J.G. van Sloun is also with Phillips Research, Eindhoven, The Netherlands.

the severity of the involved risks, deep learning models that appropriately deal with aleatoric uncertainty can substantially improve clinical decision-making [12]–[14].

Presenting various plausible image segmentation hypotheses was initially enabled by the use of Monte-Carlo dropout [15], ensembling methods [16], [17], or the use of multiple classification heads [18], [19]. However, these methods approximate the weight distribution over the neural networks, i.e., the epistemic uncertainty, rather than the aleatoric uncertainty. In this context, the PU-Net made significant advances by combining the conditional Variational Autoencoder (VAE) [20], [21] and U-Net [22]. In this case, a suitable objective is derived from the ELBO of the *conditional* data log-likelihood, which is analogous to the unconditional VAE. The PU-Net is especially interesting in its application, as the low-dimensional latent densities enable interpretability and manipulation of the data, while maintaining a theoretically justified probabilistic framework with fast inference. Nonetheless, several works have recently highlighted the limitations of the PU-Net [23]–[25]. Most relevant to this work, which pertains improving the latent space, is the augmentation of Normalizing Flows to the posterior density to boost expressivity [26], [27]. Also, Bhat *et al.* [28] demonstrate changes in model performance subject to density modeling design choices. Beyond this, the latent-space behaviour of the PU-Net has, to the best of our knowledge, not received much attention.

In this work, we find that the latent space can possess properties that inhibit aleatoric uncertainty quantification. Specifically, the learned latent space variances are significantly

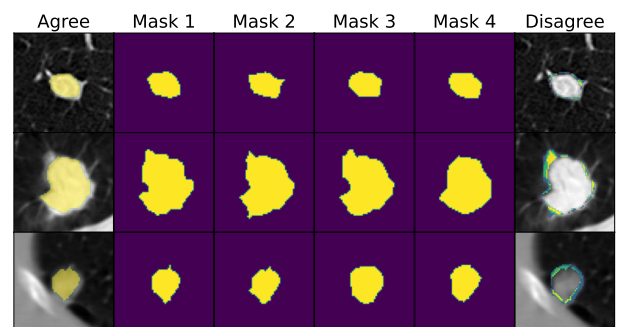


Fig. 1: Samples of the LIDC-IDRI dataset with significant inter-observer variability where (dis-)agreement in the ground-truth masks is clearly visible.

sparse. This under-utilization of the latent space can indicate that a substantial amount of information from the posterior is simply ignored. As a consequence, the inhomogeneous latent variance distribution causes the network to be ill-conditioned, resulting in inefficient and unstable gradient descent updates. While this issue is a general concern, its significance within medical settings is particularly pronounced, as underscored by clinical research [10], [11], [29]–[33]

In our experiments, we address this challenge by maximizing the mutual information between the segmentation masks and latent space. This enables the introduction of a new model, the Sinkhorn PU-Net (SPU-Net), which training objective also uses entropy-regularized Sinkhorn Divergence. Both mutual information maximization and entropy regularization encourage homogeneity in the latent-density singular values, which causes the decoder to be better conditioned and leading to more effective gradient-descent optimization. As such, the encapsulation of the inter-observer variability is significantly improved. To summarize, the contributions of this work are:

- Providing detailed insights into the effect of singular values on the quantification of aleatoric uncertainty with conditional latent density models.
- Introducing a new training methodology that significantly improves (up to 11%) upon preceding latent variable models for probabilistic segmentation.

The remainder of this paper is structured as follows. First, we present various theoretical frameworks in Section II. These sections serve as a foundation for our proposed methodology in Section III. Then, quantitative and qualitative results of the conducted experiments are presented and discussed in Section IV. Limitations of our work are mentioned in Section V and finally, conclusions are drawn in Section VI.

II. THEORETICAL BACKGROUND

This section first provides an introduction to aleatoric uncertainty quantification in segmentation. Then, the VAE and PU-Net are introduced, where both models maximize a lower-bound on the data log-likelihood. We subsequently mention several challenges that can arise during this optimization process. Additionally, the theory of Optimal Transport will be presented with the intention to enable the use of alternative divergence measures in latent space. In the remainder of this paper, we will use calligraphic letters (\mathcal{X}) for sets, capital letters (X) for random variables, and lowercase letters (x) for specific values. Furthermore, we will denote marginals as P_X , probability distributions as $P(X)$, and densities as $p(x)$. Vectors and matrices are distinguished with **boldface** characters.

A. Aleatoric uncertainty quantification

Conventional deterministic deep learning models attempt to find function $F : \mathcal{X} \rightarrow \mathcal{Y}$, to map input image $\mathbf{X} \in \mathcal{X}$ to segmentation $\mathbf{Y} \in \mathcal{Y}$. In truth, data is inherently ambiguous and annotators can differ in opinion due to varying experience and expertise. This challenges the assumptions of gold-standard annotations and suggests a probabilistic relationship between

the images and segmentation masks. This is most evident in multi-annotated datasets. Probabilistic segmentation aims to capture this relationship through an approximate density $p_\theta(\mathbf{y}|\mathbf{x})$, parameterized by θ . The simplest and most straightforward approach is interpreting the pixel-wise SoftMax values as parameters of a probability mass function. However, such models can not sample coherent segmentation masks.

Therefore, a wide spectrum of techniques have been developed to address aleatoric uncertainty quantification in segmentation, each offering its unique strengths and limitations, making the selection of methods contingent upon the specific demands and constraints of downstream tasks. The current state-of-art is held by Diffusion Denoising Probabilistic Models (DDPMs) [34]–[36]. Nevertheless, DDPMs are hampered by their time-consuming Markovian sampling procedure, rendering them impractical for the validation of extensive datasets and real-time uncertainty estimation. Naturally, a substantial portion of research on DDPMs is devoted to optimizing and accelerating their inference process [37], [38].

Models based on Generative Adversarial Networks [25] are relatively fast, but trade off explicit density estimation and training stability. While Stochastic Segmentation Networks [39] demonstrate comparable performance to DDPMs, it is essential to recognize their substantial memory requirements, particularly in modeling the covariance matrix, which scales with the dimensionality of the data.

VAE-based methods [24], [40], which are the focus of our investigation, exhibit notable advantages. Such models offer a probabilistic framework by using tractable latent representation, ultimately resulting in a semantically interpretable and interpolatable data representation, paired with fast inference.

Another notable approach includes test-time augmentation [41], which is used to explore the locality of the likelihood function to obtain segmentations. Nonetheless, it has not yielded results equivalent to those achieved by other methods. Auxiliary networks have also been used to model annotation variability [42], [43], but are beyond the scope of aleatoric uncertainty quantification.

In light of this extensive array of approaches and the inherent strengths and limitations associated with each, it is crucial to focus our efforts on addressing the shortcomings of preferred models for the downstream application, contributing to the advancement of the field. Notably, models VAE-based models like the PU-Net [40] have gained popularity due to the mentioned benefits and the adaptability subject to diverse datasets. This widespread adoption underscores their appeal in the research community [24], [26], [27], [44], [45].

B. Variational Autoencoders

Let $\mathbf{X} \in \mathcal{X}$ be an observable variable, taking values in \mathbb{R}^D . We define $\mathbf{Z} \in \mathcal{Z}$ as a latent, lower-dimensional representation of \mathbf{x} , taking values in \mathbb{R}^d . It is assumed that \mathcal{X} possesses a low-dimensional structure in \mathbb{R}^r , relative to the high-dimensional ambient space \mathbb{R}^D . Thus, it is assumed that $D \gg d \geq r$. In other words, the latent dimensionality d is greater than the intrinsic dimensionality r of the data. The VAE [20] aims to approximate the data distribution through \mathbf{z} , by maximizing

the Evidence Lower Bound (ELBO) on the data log-likelihood, described by

$$\begin{aligned} \log p(\mathbf{x}) &\geq \mathbb{E}_{q_{\theta}(\mathbf{z}|\mathbf{x})} \left[\log \frac{p(\mathbf{x}, \mathbf{z})}{q_{\theta}(\mathbf{z}|\mathbf{x})} \right] \\ &\geq \mathbb{E}_{q_{\theta}(\mathbf{z}|\mathbf{x})} [\log p_{\phi}(\mathbf{x}|\mathbf{z})] - \text{KL} [q_{\theta}(\mathbf{z}|\mathbf{x}) || p(\mathbf{z})], \end{aligned} \quad (1)$$

with tractable encoder $q_{\theta}(\mathbf{z}|\mathbf{x})$ (commonly known as the posterior) and decoder $p_{\phi}(\mathbf{x}|\mathbf{z})$ densities, amortized with parameters θ and ϕ , respectively. Furthermore, $p(\mathbf{z})$ is a fixed latent density and is commonly referred to as the prior. As a consequence of the mean-field approximation, the densities are modeled with axis-aligned Normal densities. Furthermore, to enable prediction from test images, optimization is performed through amortization with neural networks. Nevertheless, due to these approximations, this construction can be sub-optimal, reduce the effectiveness of the VAE and void the guarantee that high ELBO values indicate accurate inference [46], [47].

C. The Probabilistic U-Net

Similar to the VAE, consider input image and ground-truth segmentation masks $\mathbf{X}, \mathbf{Y} \in \mathbb{R}^D$. Then, the ELBO of the *conditional* data log-likelihood can be written as

$$\begin{aligned} \log p(\mathbf{y}|\mathbf{x}) &\geq \mathbb{E}_{q_{\theta}(\mathbf{z}|\mathbf{x}, \mathbf{y})} \left[\log \frac{p(\mathbf{y}, \mathbf{z}|\mathbf{x})}{q_{\theta}(\mathbf{z}|\mathbf{y}, \mathbf{x})} \right] \\ &\geq \mathbb{E}_{q_{\theta}(\mathbf{z}|\mathbf{x}, \mathbf{y})} [\log p_{\phi}(\mathbf{y}|\mathbf{x}, \mathbf{z})] \\ &\quad - \text{KL} [q_{\theta}(\mathbf{z}|\mathbf{y}, \mathbf{x}) || p_{\psi}(\mathbf{z}|\mathbf{x})], \end{aligned} \quad (2)$$

and the predictive distribution from test image \mathbf{x}^* as

$$p(\mathbf{y}|\mathbf{x}^*) := \int_{\mathbb{R}^d} p_{\phi}(\mathbf{y}|\mathbf{z}, \mathbf{x}^*) p_{\psi}(\mathbf{z}|\mathbf{x}^*) d\mathbf{z}. \quad (3)$$

The success of the PU-Net for probabilistic segmentation can be accredited to several additional design choices in the implementation of the encoding-decoding structure. Firstly, an encoding \mathbf{z} , is inserted pixel-wise at the final stages of a U-Net, followed by feature-combining 1×1 convolutions only. As a result, this significantly alters the r -dimensional manifold that \mathbf{z} attempts to learn. Namely, it learns the segmentation variability within a single image rather than features of the segmentation itself. Therefore, much smaller values of d are feasible. Another crucial difference in the PU-Net formulation w.r.t. to that of the VAE is the conditioning of the prior $p_{\psi}(\mathbf{z}|\mathbf{x})$, which is not fixed but rather learned. Although it has been argued by Zheng *et al.* [48] that learning the prior density is theoretically equivalent to using a non-trainable prior, their respective optimization trajectories can differ substantially such that the former method is preferred [23], [24], [40].

D. Challenges with latent variable models

1) *Information preference*: A common hurdle when training the VAE is the phenomena of ignored latent codes [46], [49]. While ignored latent variables can potentially produce realistic looking samples, it completely undermines its inference capabilities relevant for downstream tasks. This problem was initially recognized when strong networks such as Recurrent Neural Networks (RNNs) were used as decoders [50]–[52]. A

common hypothesis argues that early on during training, the latent codes \mathbf{z} carry negligible information on \mathbf{x} . Therefore, the prior regularization term in the ELBO the objective can be easily minimized. Chen *et al.* [49] describe that this problem is not solely related to optimization, but can generally occur subject to intractable true posteriors and powerful decoders. Zhao *et al.* [46] also demonstrate that the ELBO can reach global optimum without utilizing the latent codes. The PU-Net, an extension of the ELBO to the conditional case, can therefore suffer from similar issues such that it defaults to non-informative latent variables.

2) *Learnable priors*: Instead of fixing the prior, learning this density has shown commendable results. Nonetheless, such modeling choice can exacerbate collapse to degenerate solutions with uninformative latent variables. Consider the KL-divergence between two d -dimensional axis-aligned Normals \mathcal{N}_1 and \mathcal{N}_2 with identical means

$$2 \cdot \text{KL} [\mathcal{N}_1 || \mathcal{N}_2] = \sum_i \frac{\sigma_2^i}{\sigma_1^i} + \ln \frac{\sigma_1^i}{\sigma_2^i} - d. \quad (4)$$

Minimizing this expression entails finding $\sigma_1^i = \sigma_2^i$ for all values of i . At the same time, the singular values are progressively minimized [48] and the variance vectors σ_1 and σ_2 are not constrained in any fashion. This means the variances can be arbitrarily distributed, including low-entropy solutions (i.e. sparse) where the latent space is completely ignored except for some dimension that governs the required stochasticity to satisfy the reconstruction cost in Equation (2).

3) *Decoder sensitivity*: A sparse latent representation can cause the decoder to become extremely sensitive to the latent-space sample localization. The PU-Net decoder is dependent on the function $\mathbf{f}_{\phi}(\mathbf{x}, \mathbf{z})$, where $p_{\phi}(\mathbf{y}|\mathbf{x}, \mathbf{z}) = \delta(\mathbf{y} - \mathbf{f}_{\phi}(\mathbf{x}, \mathbf{z}))$, which intermediately involves latent variable \mathbf{z} to reconstruct a plausible segmentation hypothesis. The latent variable \mathbf{z} is controlled by the mean μ and singular values σ of the underlying axis-aligned Normal density. If the input \mathbf{x} is considered to be fixed, then the relative condition number, ζ_i , of $\mathbf{f}_{\phi}(\mathbf{x}, \mathbf{z})$ can be interpreted as the sensitivity of its output w.r.t. its varying input z_i , corresponding to the i -th latent dimension, which can be expressed as

$$\zeta_i = \lim_{\epsilon \rightarrow 0} \sup_{\|\delta z_i\| \leq \epsilon} \frac{\|\delta \mathbf{f}_{\phi}(\mathbf{x}, z_i)\| / \|\mathbf{f}_{\phi}(\mathbf{x}, \mathbf{z})\|}{\|\delta z_i\| / \|\mathbf{z}\|}. \quad (5)$$

For convenient notation, only the varying z_i is included in $\delta \mathbf{f}_{\phi}(\mathbf{x}, z_i)$ rather than the complete vector \mathbf{z} . The condition number of a function has direct consequences to the numerical stability of its gradient updates. Suppose $\sigma_1 \gg \sigma_2$ and $\mu_1 \approx \mu_2$, then $\zeta_2 \gg \zeta_1$, and the function is said to be ill-conditioned. To illustrate with a simplification, consider function

$$f(z_1, z_2) = w_1 z_1 + w_2 z_2 \quad (6)$$

with weights w_1 and w_2 , and latent variables z_1 and z_2 . The subsequent gradients are

$$\nabla f = \left[\frac{\partial f}{\partial w_1}, \frac{\partial f}{\partial w_2} \right]^T = [z_1, z_2]^T. \quad (7)$$

It can be seen that the gradients updates are governed by the magnitudes of z_1 and z_2 . Hence, the case $\sigma_1 \gg \sigma_2$

(the underlying variances of z) will skew the optimization landscape, where the gradients w.r.t. z_2 will dominate, leading to inefficient and unstable gradient descent updates. When considering that the dimensionality is usually higher than $d = 2$, the search towards an optimal minimum will rapidly suffer from irregular condition numbers [53].

In conventional convex optimization, the Newton’s method is used to consider curvature of the optimization landscape, appropriately dealing with inefficient gradient updates due to skewness. In complex and deep neural networks, normalization layers have been used in neural networks to smoothen optimization and have led to considerable improvements [54]–[58]. In the case of latent variable modeling, this pertains stimulating latent variances which are approximately of the same magnitude.

4) *Augmentation with Normalizing Flows*: Furthermore, past literature has made mention of enhancing the posterior density by augmentation of Normalizing Flows [59], which was proposed to enhance the expressivity and complexity of the posterior distribution to reduce the amortization gap [47]. This has shown to improve the PU-Net [26], [27]. Nevertheless, it has been argued in previous works that the mean-field Gaussian assumption in the VAE is not necessarily the cause for the failure to learn the ground-truth manifold [60]. Thus, further exploration on the effects on a NF-augmented posterior is required.

E. Optimal Transport

Let \mathcal{Y} and $\hat{\mathcal{Y}}$ be the two separable metric spaces. For the sake of clarity, the reader can assume that these sets contain the ground-truth and model predictions, respectively. We adopt the Monge-Kantorovich formulation [61] for the OT problem, by specifying

$$W(\mu, \hat{\mu}) := \inf \left\{ \int_{\mathcal{Y} \times \hat{\mathcal{Y}}} c(\mathbf{y}, \hat{\mathbf{y}}) d\gamma(\mathbf{y}, \hat{\mathbf{y}}) \mid \gamma \in \Gamma(\mu, \hat{\mu}) \right\}, \quad (8)$$

where $\gamma \in \Gamma(\mu, \hat{\mu})$ denotes a coupling in the tight collection of all probability measures on $\mathcal{Y} \times \hat{\mathcal{Y}}$ with marginals μ and $\hat{\mu}$, respectively. The function $c(\mathbf{y}, \hat{\mathbf{y}}): \mathcal{Y} \times \hat{\mathcal{Y}} \rightarrow \mathbb{R}_+$ denotes any lower semi-continuous measurable cost function. Equation (8) is also commonly referred to as the Wasserstein distance. Furthermore, the usual context of this formulation is in finding the lowest cost of moving samples from the probability measures in \mathcal{Y} to the measures in $\hat{\mathcal{Y}}$. In the case of probabilistic segmentation, the aim is to learn the ground-truth distribution $P_{Y|X}$, by matching it with the model distribution $P_{\hat{Y}|X}$. The Wasserstein distance is in practice a tedious calculation. As a solution, it has been proposed to introduce entropic regularization [62]. This is achieved by using the entropy of the couplings γ as a regularizing function, which is specified by

$$\tilde{S}_\epsilon(\mu, \hat{\mu}) := \inf \left\{ \int_{\mathcal{Y} \times \hat{\mathcal{Y}}} s(\mathbf{y}, \hat{\mathbf{y}}) d\gamma(\mathbf{y}, \hat{\mathbf{y}}) \mid \gamma \in \Gamma(\mu, \hat{\mu}) \right\}, \quad (9)$$

where

$$s(\mathbf{y}, \hat{\mathbf{y}}) = d(\mathbf{y}, \hat{\mathbf{y}}) + \epsilon \log \frac{d\gamma(\mathbf{y}, \hat{\mathbf{y}})}{d\mu(\mathbf{y})d\hat{\mu}(\hat{\mathbf{y}})}. \quad (10)$$

As mentioned by Cuturi *et al.* [63], the entropy term can be expanded to $\log(d\gamma(\mathbf{y}, \hat{\mathbf{y}})) - \log(d\mu(\mathbf{y})) - \log(d\hat{\mu}(\hat{\mathbf{y}}))$. Cuturi *et al.* [63] show that this entropic regularization allows optimization over a Lagrangian dual for faster computation with the iterative Sinkhorn matrix scaling algorithm. Additionally, the entropic bias is removed from the OT problem to obtain the Sinkhorn Divergence, specified as

$$S_\epsilon(\mu, \hat{\mu}) = \tilde{S}_\epsilon(\mu, \hat{\mu}) - \frac{1}{2} \left(\tilde{S}_\epsilon(\mu, \mu) + \tilde{S}_\epsilon(\hat{\mu}, \hat{\mu}) \right). \quad (11)$$

The Sinkhorn Divergence interpolates between W_p when $\epsilon \rightarrow 0$ with $\mathcal{O}(\epsilon \log(\frac{1}{\epsilon}))$ deviation, and Maximum Mean Discrepancy when $\epsilon \rightarrow \infty$, which favours dimension-independent sample complexity [64]. A viable option is to approximate the Sinkhorn Divergence via sampling with weights $\alpha, \beta \in \mathbb{R}_+$. To increase efficiency and speed, Kosowsky and Yuille [65] introduce ϵ -scaling or *simulated annealing* to the Sinkhorn algorithm, which implies letting ϵ decrease across iterations.

The entropic regularization can be understood as constraining the joint probability distribution to have *sufficient entropy*, or contain small enough *mutual information* with respect to $d\mu$ and $d\hat{\mu}$. Assuming normally distributed joint density \mathcal{N} with covariance Σ for the sake of analysis, the mutual information in the case of identical means becomes

$$I(\mathbf{z}_1, \mathbf{z}_2) = D_{KL}[\mathcal{N} \parallel \mathcal{N}_1 \mathcal{N}_2] = \frac{\det \Sigma_1 \det \Sigma_2}{\det \Sigma}, \quad (12)$$

with Σ being the covariance of the joint probability density. This can be considered as a multivariate correlation measure, as the expression in the case of $d = 1$ reduces to $\log \sqrt{\frac{1}{1-r^2}}$, where r is the correlation coefficient. Thus, strong correlation between the posterior and prior latent variables will be penalized by entropic regularization, preventing collapse to low-entropy solutions and as mentioned in Section II-D3, will improve gradient descent updates.

Various works have investigated constraining the latent densities by means of Optimal Transport [66]. Tolstikhin *et al.* [67] introduce Wasserstein Autoencoders (WAEs), which softly constrain the latent densities with a Wasserstein penalty term, a metric that emerged from OT theory [68]. The authors demonstrate that the WAEs exhibit better sample quality while maintaining the favourable properties of the VAE. Similarly, Patrini *et al.* [69] introduce the Sinkhorn Autoencoder (SAE), in which the Sinkhorn algorithm [63] – an approximation of the Wasserstein distance – is leveraged as a latent divergence measure. The aforementioned research has been conducted in the setting of a VAE with an unconditional ELBO objective. The PU-Net architecture, on the other hand, is an extension of the cVAE, which employs the conditional ELBO with a learnable prior density and alters the nature of the training objective.

III. METHODS

It has been argued that the PU-Net can converge to sub-optimal latent representations due ignoring information of

the posterior latent distribution, which continuously inhibits gradient descent optimization. To approach this challenge, we present a general implementation that maximizes the mutual information between the latent space and segmentation masks. To address potentially inhomogenous latent space variances, we propose the use of the Sinkhorn Divergence, which is strongly guided by entropic regularization and further encourages latent space homogeneity.

A. Maximizing Mutual information

The ELBO can be rewritten as

$$\begin{aligned}
\log p(\mathbf{y}|\mathbf{x}) &\geq \mathbb{E}_{q_{\theta}(\mathbf{z}|\mathbf{y},\mathbf{x})} \left[\log \frac{p(\mathbf{y}, \mathbf{z}|\mathbf{x})}{q_{\theta}(\mathbf{z}|\mathbf{y}, \mathbf{x})} \right] \\
&= \mathbb{E}_{q_{\theta}(\mathbf{z}|\mathbf{y},\mathbf{x})} [\log p_{\phi}(\mathbf{y}|\mathbf{x}, \mathbf{z}) - \log q_{\theta}(\mathbf{z}|\mathbf{y}, \mathbf{x}) \\
&\quad + \log p_{\psi}(\mathbf{z}|\mathbf{x})] \\
&= \mathbb{E}_{q_{\theta}(\mathbf{z}|\mathbf{y},\mathbf{x})} \left[\log p_{\phi}(\mathbf{y}|\mathbf{x}, \mathbf{z}) \right. \\
&\quad \left. - \log \frac{q_{\theta}(\mathbf{y}|\mathbf{z}, \mathbf{x})q_{\theta}(\mathbf{z}|\mathbf{x})}{p(\mathbf{y}|\mathbf{x})} + \log p_{\psi}(\mathbf{z}|\mathbf{x}) \right] \\
&= \mathbb{E}_{q_{\theta}(\mathbf{z}|\mathbf{y},\mathbf{x})} \left[\log p_{\phi}(\mathbf{y}|\mathbf{x}, \mathbf{z}) + \log \frac{p_{\psi}(\mathbf{z}|\mathbf{x})}{q_{\theta}(\mathbf{z}|\mathbf{x})} \right. \\
&\quad \left. + \log \frac{p(\mathbf{y}|\mathbf{x})}{q_{\theta}(\mathbf{y}|\mathbf{z}, \mathbf{x})} \right] \\
&= \mathbb{E}_{q_{\theta}(\mathbf{z}|\mathbf{y},\mathbf{x})} \left[\log p_{\phi}(\mathbf{y}|\mathbf{x}, \mathbf{z}) + \log \frac{p_{\psi}(\mathbf{z}|\mathbf{x})}{q_{\theta}(\mathbf{z}|\mathbf{x})} \right. \\
&\quad \left. + \log \frac{q_{\theta}(\mathbf{z}|\mathbf{x})}{q_{\theta}(\mathbf{z}|\mathbf{y}, \mathbf{x})} \right] \\
&= \mathbb{E}_{q_{\theta}(\mathbf{z}|\mathbf{y},\mathbf{x})} [\log p_{\phi}(\mathbf{y}|\mathbf{x}, \mathbf{z})] \\
&\quad - \text{KL}[q_{\theta}(\mathbf{z}|\mathbf{x})||p_{\psi}(\mathbf{z}|\mathbf{x})] - I(\mathbf{y}, \mathbf{z}|\mathbf{x}). \quad (13)
\end{aligned}$$

Note how the mutual information is naturally minimized. For the eventual segmentation task, good reconstruction and an *aggregate* posterior, $q_{\theta}(\mathbf{z}|\mathbf{x})$, congruent with the prior is essential. However, the mutual information term, which can cause uninformative latent variables, is not crucial. Hence, we inverse the contribution of the mutual information $I(\mathbf{y}, \mathbf{z}|\mathbf{x})$ and introduce the hyperparameters α and β similar to related literature [70]. We obtain the minimization objective

$$\begin{aligned}
\mathcal{L} &= -\mathbb{E}_{q_{\theta}(\mathbf{z}|\mathbf{y},\mathbf{x})} [\log p_{\phi}(\mathbf{y}|\mathbf{x}, \mathbf{z})] + \\
&\quad \beta \cdot \text{KL}[q_{\theta}(\mathbf{z}|\mathbf{x})||p_{\psi}(\mathbf{z}|\mathbf{x})] - \alpha \cdot I(\mathbf{y}, \mathbf{z}|\mathbf{x}) \\
&= -\mathbb{E}_{q_{\theta}(\mathbf{z}|\mathbf{y},\mathbf{x})} \left[\log p_{\phi}(\mathbf{y}|\mathbf{x}, \mathbf{z}) + \beta \cdot \log \frac{q_{\theta}(\mathbf{z}|\mathbf{x})}{p_{\psi}(\mathbf{z}|\mathbf{x})} \right] \\
&\quad - \alpha \cdot I(\mathbf{y}, \mathbf{z}|\mathbf{x}) \\
&= -\mathbb{E}_{q_{\theta}(\mathbf{z}|\mathbf{y},\mathbf{x})} \left[\log p_{\phi}(\mathbf{y}|\mathbf{x}, \mathbf{z}) + \beta \cdot \log \frac{q_{\theta}(\mathbf{z}|\mathbf{x})}{p_{\psi}(\mathbf{z}|\mathbf{x})} \right. \\
&\quad \left. + \alpha \cdot \log \frac{q_{\theta}(\mathbf{z}|\mathbf{x})}{q_{\theta}(\mathbf{z}|\mathbf{y}, \mathbf{x})} \right] \\
&= -\mathbb{E}_{q_{\theta}(\mathbf{z}|\mathbf{y},\mathbf{x})} \left[\log p_{\phi}(\mathbf{y}|\mathbf{z}, \mathbf{x}) + \log \frac{q_{\theta}(\mathbf{z}|\mathbf{x})^{\beta+\alpha}}{p_{\psi}(\mathbf{x}|\mathbf{z})^{\beta} q_{\theta}(\mathbf{z}|\mathbf{y}, \mathbf{x})^{\alpha}} \right] \\
&= -\mathbb{E}_{q_{\theta}(\mathbf{z}|\mathbf{y},\mathbf{x})} [\log p_{\phi}(\mathbf{y}|\mathbf{x}, \mathbf{z})] \\
&\quad + \alpha \cdot \text{KL}[q_{\theta}(\mathbf{z}|\mathbf{y}, \mathbf{x})||p_{\psi}(\mathbf{z}|\mathbf{x})] \\
&\quad + \beta \cdot \text{KL}[q_{\theta}(\mathbf{z}|\mathbf{x})||p_{\psi}(\mathbf{z}|\mathbf{x})]. \quad (14)
\end{aligned}$$

In the next section, we will justify constraining the aggregate posterior $q_{\theta}(\mathbf{z}|\mathbf{x})$ with the Sinkhorn Divergence by taking the OT perspective on this segmentation problem.

B. Sinkhorn Divergence on the aggregated posterior

It has been shown in the previous section that the training objective can be modified to contain the KL-divergence with the aggregated posterior. By using the theoretical framework of Bousquet *et al.* [66], we will show that this constraint on the aggregated posterior can be an OT solution. Most works employ this technique to provide an alternative to the conventional VAE objective [67], [69]. We specifically consider the optimization problem in the conditional setting for probabilistic segmentation and have framed previous literature accordingly to this context.

Consider the random variables $(\mathbf{X}, \mathbf{Y}, \hat{\mathbf{Y}}, \mathbf{Z}) \in \mathcal{X} \times \mathcal{Y} \times \mathcal{Y} \times \mathcal{Z}$, which correspond to the input image, ground-truth segmentation, model prediction and latent code, respectively. Then, we denote the joint distribution $P_{\mathbf{Y}, \mathbf{Z}|\mathbf{X}}$, where a latent variable is obtained as $\mathbf{Z} \sim P_{\mathbf{Z}|\mathbf{X}}$, and ground truth is obtained with $\mathbf{Y} \sim P_{\mathbf{Y}|\mathbf{Z}, \mathbf{X}}$. The OT problem considers couplings $\Gamma(\mathbf{Y}, \hat{\mathbf{Y}}|\mathbf{X}) = \Gamma(\hat{\mathbf{Y}}|\mathbf{Y}, \mathbf{X})P(\mathbf{Y}|\mathbf{X})$, where $\Gamma(\hat{\mathbf{Y}}|\mathbf{Y}, \mathbf{X})$ can be factored with a non-deterministic mapping through latent variable \mathbf{Z} , as is shown by Bousquet *et al.* [66]. In fact, considering a probabilistic encoder $Q_{\mathbf{Z}|\mathbf{Y}, \mathbf{X}}$, deterministic decoder f_{ϕ} and the set of joint marginals $\mathcal{P}_{\mathbf{Y}, \mathbf{Z}|\mathbf{X}}$, the optimal solution of the OT problem can be stated as

$$\begin{aligned}
W(P_{\mathbf{Y}|\mathbf{X}}, P_{\hat{\mathbf{Y}}|\mathbf{X}}) &= \inf_{P \in \mathcal{P}_{\mathbf{Y}, \mathbf{Z}|\mathbf{X}}} \mathbb{E}_{P_{\mathbf{Y}, \mathbf{Z}|\mathbf{X}}} [c(\mathbf{Y}, f_{\phi}(\mathbf{Z}, \mathbf{X}))] \quad (15a)
\end{aligned}$$

$$= \inf_{Q: Q_{\mathbf{Z}|\mathbf{X}} = P_{\mathbf{Z}|\mathbf{X}}} \mathbb{E}_{P_{\mathbf{Y}|\mathbf{X}}} \mathbb{E}_{Q_{\mathbf{Z}|\mathbf{Y}, \mathbf{X}}} [c(\mathbf{Y}, f_{\phi}(\mathbf{Z}, \mathbf{X}))], \quad (15b)$$

with prior and aggregated posterior, $P_{\mathbf{Z}} = P(\mathbf{Z}|\mathbf{X})$ and $Q_{\mathbf{Z}|\mathbf{X}} = \mathbb{E}_{P_{\mathbf{Y}|\mathbf{X}}} [Q(\mathbf{Z}|\mathbf{Y}, \mathbf{X})]$, respectively (see Theorem 1 of Bousquet *et al.* [66] for further details). Equation (15a) follows by definition and Equation (15b) indicates that rather than finding the couplings Γ , the search can be factored through probabilistic encoders Q which attempts to match the marginal $P_{\mathbf{Z}}$. Continuously, the constraint on the aggregated marginals can be relaxed with a convex penalty $D: \mathcal{Q} \times \mathcal{P} \rightarrow \mathbb{R}_{+}$ such that $D(Q_{\mathbf{Z}|\mathbf{X}}, P_{\mathbf{Z}|\mathbf{X}}) = 0$ if, and only if $Q_{\mathbf{Z}|\mathbf{X}} = P_{\mathbf{Z}|\mathbf{X}}$.

A viable option for this penalty is the Sinkhorn Divergence [63], which is convex, smooth and positive definite [71] and can serve as a surrogate for the KL-divergence on the aggregated posterior in Equation (14). Furthermore, the entropic regularization can reduce the models susceptibility to collapse to low-entropy solutions, as has been discussed in Section II-E. The novel minimization objective, which is named the Sinkhorn PU-Net (SPU-Net) for reference, can be stated as

$$\begin{aligned}
\mathcal{L} &= -\mathbb{E}_{q_{\theta}(\mathbf{z}|\mathbf{y},\mathbf{x})} [\log p_{\phi}(\mathbf{y}|\mathbf{x}, \mathbf{z})] \\
&\quad + \alpha \cdot \text{KL}[q_{\theta}(\mathbf{z}|\mathbf{y}, \mathbf{x})||p_{\psi}(\mathbf{z}|\mathbf{x})] \\
&\quad + \beta \cdot S_{\epsilon}[q_{\theta}(\mathbf{z}|\mathbf{x})||p_{\psi}(\mathbf{z}|\mathbf{x})], \quad (16)
\end{aligned}$$

where α and β are tunable parameters.

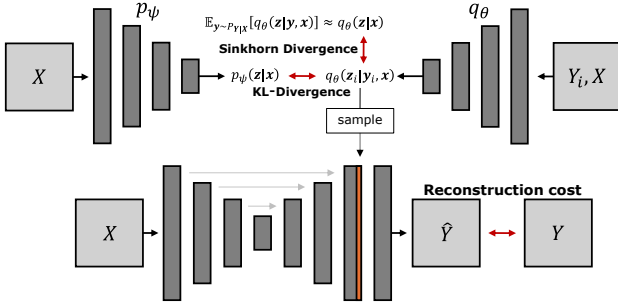


Fig. 2: Schematic drawing of the Sinkhorn Probabilistic U-Net (SPU-Net) training framework, which is an extension of the PU-Net introduced by Kohl *et al.* [40]. The ground truth is denoted as \mathbf{Y} , the input image as \mathbf{X} , and the model prediction as $\hat{\mathbf{Y}}$. During testing, only the prior density $p_\psi(\mathbf{z}|\mathbf{x})$ is used to predict samples.

Dataset	Modality	Annotators	samples
LIDC-IDRI	CT	4	15096
QUBIQ	Pancreas	2	702
	Pancreatic lesion	2	206

TABLE I: Modality, number of annotators and size for the used datasets.

C. Data

This study employs a diverse range of post-processed, multi-annotated medical image segmentation datasets, which exhibit significant variations in the ground truth, to train and evaluate the proposed models. Furthermore, the utilization of publicly available datasets underscores the clinical significance of this research. Firstly, we use the LIDC-IDRI [72] dataset, a popular benchmark for aleatoric uncertainty quantification, which contains lung-nodule CT scans. Secondly, we use the Pancreas, Pancreatic-lesion CT datasets provided by the QUBIQ 2021 Challenge [73]. See Table I for an overview. Some datasets of the QUBIQ challenge are omitted due to their tiny sizes, which makes training unstable, evaluation extremely sensitive to a few test samples and inhibit meaningful analysis.

In line with related literature, it is assumed that the region of interest is detected and the desired uncertainty is solely regarding its exact delineation. This is also common practise in clinical procedures, where initially detection of lesions are considered, only to be then followed by more precise characterization [74]–[78]. Therefore, each image is center-cropped to 128×128 -pixel patches. Furthermore, a train/validation/test set is exploited where approximately 20% of the dataset is reserved for testing and three-fold cross-validation is used on the remaining 80%. We carefully split the data according to patient number to avoid data leakage or model bias.

D. Training

The proposed SPU-Net is compared to the PyTorch implementation of the PU-Net [40] and its NF-augmented variant (with a 2-step planar flow) [26], which we will refer to as the

PU-Net+NF. We point readers to the respective papers for further details on both the PU-Net and PU-Net+NF architectures, which also serve as the foundation of the SPU-Net.

Optimizing Equation (16) involves the aggregate posterior, i.e. integration over all segmentation masks. The aggregated posterior can be approximated as $q_\theta(\mathbf{z}|\mathbf{x}) \approx \mathbb{E}_{p_{\mathbf{Y}|\mathbf{X}}}[q_\theta(\mathbf{z}|\mathbf{y}, \mathbf{x})]$. A sample of each posterior is taken and their Sinkhorn Divergence with the equivalent number of samples from the prior is determined. A randomly selected posterior is used for the reconstruction loss (cross-entropy) and analytical KL divergence with the input conditional prior $p_\psi(\mathbf{z}|\mathbf{x})$. The training procedure is shown with pseudocode in Algorithm 1.

For each dataset, we train the PU-Net, PU-Net+NF and our proposed method. Each of those models are trained on three folds using cross-validation. Furthermore, the experiments per model and dataset are conducted across four latent dimensions. All hyperparameters across experiments are kept identical, except for the number of training epochs and parameters related to the Sinkhorn Divergence. This implies across all datasets a batch size of 32, using the Adam optimizer with a maximum learning rate of 10^{-4} that is scheduled by a linear warm-up of 5 and 50 epochs for the LIDC-IDRI and QUBIQ datasets, respectively, cosine annealing, and weight decay of 10^{-5} . For our proposed method, we additionally constraint the gradient to unitary norm. For the LIDC-IDRI dataset we set the number of training epochs to 200 and for all QUBIQ datasets we trained for 2,500 epochs. After training, we used the model checkpoint with the lowest validation loss. This was usually much earlier than the set number of iterations. To implement the Sinkhorn Divergence, we make use of the `GeomLoss` [71] package.

Furthermore, data augmentation has been used during training, which consisted of random rotations within $[-180, 180]$ degrees, scaling within $[0.8, 1.2]$, and translation and shears in all directions of 0.1 and 30%, respectively. The number of samples taken from the densities equal the number of available segmentation masks from each dataset.

Algorithm 1: Pseudocode of the proposed training algorithm

- 1 $\mathcal{Y} \sim p_{\mathbf{Y}|\mathbf{X}}$;
 - 2 $k \leftarrow \text{random.int}(n_masks)$;
 - 3 **forall** $\mathbf{y} \in \mathcal{Y}$ **do**
 - 4 $\mathbf{z}_i^\theta \sim q_\theta(\mathbf{z}|\mathbf{x}, \mathbf{y})$;
 - 5 $\mathbf{z}_i^\psi \sim p_\psi(\mathbf{z}|\mathbf{x})$;
 - 6 $\hat{\mathbf{y}} \sim p_\phi(\mathbf{y}|\mathbf{x}, \mathbf{z}_k^\theta)$;
 - 7 $loss \leftarrow \text{CE}(\mathbf{y}_k, \hat{\mathbf{y}}) + \text{KL}(q_\theta, q_\psi) + \text{Sinkhorn}(\mathbf{z}^\theta, \mathbf{z}^\psi)$;
-

E. Evaluation

1) *Data distribution*: To evaluate the model performances, Hungarian Matching has recently been used as an alternative to the Generalized Energy Distance (GED). This, because the GED can be biased to simply reward sample diversity when subject to samples of poor quality [24], [26]. We refer to

Hungarian Matching as the Empirical Wasserstein Distance, abbreviated as EWD or \hat{W}_k , since it is essentially equivalent to the Wasserstein distance between the discrete set of samples from the model and the ground-truth distribution. Hence, the EWD is a well-suited metric, since the latent samples are attempted to be matched in a similar fashion as when using the Sinkhorn Divergence.

We implement the EWD as follows. Each set of ground-truth segmentations are multiplied to match the number of predictions N obtained during testing. We then apply a cost metric k to each combination of elements in the ground-truth and prediction set, to obtain an $N \times N$ cost matrix. Subsequently, the unique optimal coupling between the two sets that minimizes the average cost is determined. We use unity minus the Intersection over Union (1 - IoU) as cost function for k . We assign maximum score for correct empty predictions, which implies zero for the EWD. We sample 16 predictions for the LIDC-IDRI, Pancreas and Pancreatic-lesion dataset, which were specifically chosen to be multiples of the number of available annotations.

2) *Latent distribution*: The method used to determine the latent space homogeneity is the Effective Rank (ER) [79], which can be regarded as an extension of the conventional matrix rank. The ER is defined as

$$\text{ER}(\sigma) = e^{-\sum c_i \log c_i}, \quad (17)$$

where c_i are elements of the normalized singular values $\mathbf{c} = \frac{\sigma}{\|\sigma\|_1}$. For this approach, the singular value vector $\sigma = [\sigma_1, \sigma_2, \dots, \sigma_d]$ needs to be determined. Fortunately, the densities are axis-aligned Normals, σ can be directly obtained from the diagonal of the covariance matrix and Singular Value Decomposition is not required.

IV. RESULTS & DISCUSSION

We confirm our implementation of the baseline PU-Net with several experiments. When evaluating the PU-Net using the LIDC-IDRI dataset, we have obtained GED values of 0.327 ± 0.003 , which closely align with the reported values in the work of Kohl *et al.* [24], yet exhibit significantly reduced standard deviation. Moreover, the Hungarian-Matched IoU values surpass the values reported by Kohl *et al.* [24]. These discrepancies can be potentially attributed to differences in training splits and model initialization. Nonetheless, these findings underscore the comparable performance of our experiments, warranting a reliable basis for accurate comparison.

All models were trained on a 24GB NVIDIA RTX 3090. We show relevant statistics related to model complexity in Table III. The novel methodology does not increase the metrics with exception for training time, which increases due to additional Floating point operations per seconds (FLOPS) by approximately 1.75 w.r.t. to the baseline PU-Net. This is expected since our improved algorithm evaluated multiple posteriors in a training step. While training complexity is not the focus of this work, it is likely that evaluation in this manner can potentially reduce the number of epochs required to fully optimized the model. This, because random sampling is an approximation of the aggregated posterior.

The quantitative results from the conducted experiments are presented in Table II. Values within the range of $4 \leq d \leq 7$ have been used for the experiments. We have found values $\alpha=10$ and $\beta=100$ to sufficiently reduce the latent sparsity during training. For each dataset, the best performing model across the experimented latent dimensionalities are indicated in boldface. It can immediately be observed that the proposed method is performing best within and across each latent dimensionality in terms of aleatoric uncertainty quantification (visible from the EWD metric). Additionally, a positive correlation is apparent between the latent space homogeneity (quantified with the ER) and EWD. The algorithm evenly distributes the variances across all latent dimensionalities, which results in the best performance in terms of the EWD. This is in contrast to the PU-Net, which has a sparse latent space (i.e. low ER) and generally performed worse. The results for the PU-Net+NF support this empirical correlation as well, since its metric evaluations often reside between the former two in terms of both performance and latent space sparsity.

It is noteworthy that our methodology improves over previous literature with smaller latent dimensionalities, as this would constrain the capacity of the model. For example, our method applied on the Pancreas dataset with $d=4$ surpasses the PU-Net and PU-Net+NF with values $d \geq 4$. Similar instances can be found for the other two datasets and thus serves as evidence that the information is better captured in the latent variances of the proposed method. Furthermore, we see that the performance slightly degrades above optimal d ($d \geq r$), which has also been discussed in Dai *et al.* [60]. Nonetheless, our model still outperforms the former approaches at every dimensionality.

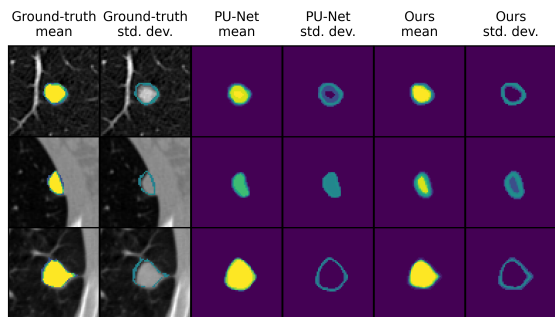
While the quantitative evaluation confirms the superior performance, clinical setting deployment will mainly entail visual evaluation. Therefore, we qualitatively inspect the mean and standard deviation of the sampled predictions of the (S)PU-Net for the various datasets in Figure 3. From the figure, the improvements in predictions over the baselines models are clearly visible. The predicted uncertainty closely matches the ground-truth, as discernible around borders of the prediction ensemble in the LIDC-IDRI dataset. For the Pancreas and Pancreatic-lesion datasets, large improvements in the mean predictions compared to the baselines can be observed. As expected, the lower EWD scores are clearly reflected in the sampled segmentation masks. These results expose the unfavourable latent space of the PU-Net.

To better understand the distribution of the latent dimensions, the mean and variances of the image-conditional prior densities are depicted in Figure 4. Here, it can clearly be seen that the PU-Net latent representation is severely sparse. In line with the previously discussed results, it can be observed that the SPU-Net has the most homogeneous prior latent density. As a consequence of mutual information maximization, we can see that the mean values are more purposeful since they are not all centered around zero.

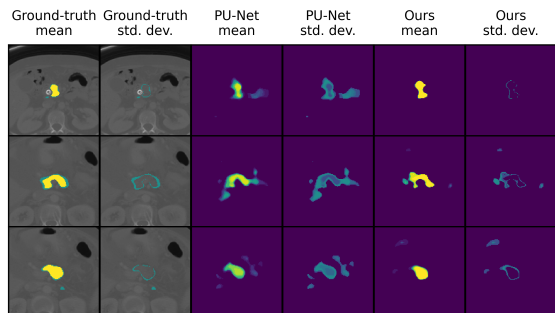
The effect of maximizing the mutual information between latent and input variables is confirmed in Figure 5. Interpolation across latent dimensions almost has no effect on the PU-Net. Interestingly enough, the figure reflects at most two

Dataset	Model	d = 4		d = 5		d = 6		d = 7	
		$\hat{W}_k \downarrow$	ER \uparrow	$\hat{W}_k \downarrow$	ER \uparrow	$\hat{W}_k \downarrow$	ER \uparrow	$\hat{W}_k \downarrow$	ER \uparrow
LIDC-IDRI	PU-Net	0.451 \pm 0.001	1.68 \pm 0.07	0.450 \pm 0.003	1.68 \pm 0.08	0.451 \pm 0.006	1.92 \pm 0.05	0.451 \pm 0.002	1.77 \pm 0.14
	PU-Net+NF	0.451 \pm 0.004	2.90 \pm 0.39	0.450 \pm 0.002	3.31 \pm 0.67	0.446 \pm 0.003	2.94 \pm 0.59	0.450 \pm 0.002	4.00 \pm 0.52
	Ours	0.447 \pm 0.005	3.52 \pm 0.04	0.441 \pm 0.002	4.57 \pm 0.03	0.440 \pm 0.006	5.12 \pm 0.10	0.443 \pm 0.002	5.59 \pm 0.06
QUBIQ Pancreas	PU-Net	0.602 \pm 0.034	1.76 \pm 0.07	0.608 \pm 0.024	1.49 \pm 0.25	0.603 \pm 0.030	1.52 \pm 0.23	0.589 \pm 0.002	1.65 \pm 0.22
	PU-Net+NF	0.581 \pm 0.004	2.37 \pm 0.24	0.610 \pm 0.080	3.15 \pm 0.43	0.585 \pm 0.021	2.77 \pm 0.24	0.589 \pm 0.054	3.77 \pm 0.98
	Ours	0.541 \pm 0.011	3.44 \pm 0.07	0.532 \pm 0.004	4.13 \pm 0.24	0.530 \pm 0.016	5.33 \pm 0.08	0.536 \pm 0.011	6.52 \pm 0.18
QUBIQ Pancreatic lesion	PU-Net	0.628 \pm 0.009	1.25 \pm 0.11	0.606 \pm 0.004	1.18 \pm 0.03	0.618 \pm 0.002	1.07 \pm 0.02	0.611 \pm 0.007	1.31 \pm 0.16
	PU-Net+NF	0.536 \pm 0.024	2.54 \pm 0.35	0.559 \pm 0.022	3.21 \pm 0.30	0.568 \pm 0.063	3.06 \pm 0.29	0.535 \pm 0.025	4.88 \pm 0.43
	Ours	0.537 \pm 0.018	3.52 \pm 0.11	0.539 \pm 0.000	4.41 \pm 0.28	0.518 \pm 0.039	4.20 \pm 0.34	0.543 \pm 0.011	5.33 \pm 0.23

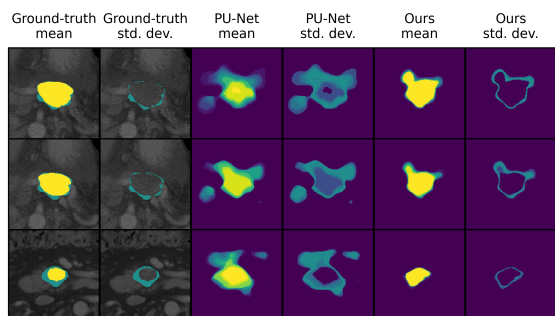
TABLE II: Comparison of the experimented models on various datasets. The PU-Net is re-implemented from [40] and PU-Net+NF from [26]. Results are evaluations on the test set. The mean and standard deviations (threefold cross-validation) of the Empirical Wasserstein metric with kernel unity minus the Intersection over Union (1-IoU) are presented. Furthermore, the homogeneity of the latent singular values are expressed with the Effective Rank. A clear relationship between a homogeneous latent space and model performance is visible.



(a) LIDC-IDRI



(b) QUBIQ Pancreas



(c) QUBIQ Pancreatic lesion

Fig. 3: Visualization of test set predictions. The mean and standard deviation is taken from 16 predictions for both PU-Net and our proposed model.

Model	Training time (appr. min/epoch)	Inference time (100 \times , s.)	Memory (GB)	Parameters (M)	FLOPS (G)
PU-Net	1.00	2.56	3.98	6.844	119
PU-Net+NF	1.13	2.57	4.07	6.853	211
Ours	1.75	2.57	4.07	6.846	350

TABLE III: Training statistics for the used models with batch size of 32. While training costs are increased, note that our methodology adds negligible costs to inference time, memory usage and parameter count.

active latent dimensions, which reflects the obtained ER of 1.92. In the proposed method, it can be observed that at least five latent dimension influence the output, which is also in line with the found result ER=5.12. This indicates that the latent space has much more influence on the output of the model.

To further investigate latent behaviour, we sequentially ‘freeze’ latent dimensions by taking its mean rather than sampling from the density in Figure 6. If the variance contribute to the output, then the model performance should degrade as dimensions are frozen. This is clearly not the case for PU-Net and is obvious for the proposed method. The diagram also reflects the found ER values in Table II.

The effect of entropy regularization on the latent codes over the course of training time is depicted in Figure 7. In all instances, it can be observed that the densities are rapidly decaying to sparse representations. This is expected due to the fact that models tend to overfit on little data and highlights the importance of data augmentation to effectively increase the dataset. The primary inquiry concerns whether data augmentation and the intrinsic variability of data suffice to elevate entropy levels as training progresses. Observations from PU-Net training indicate a failure to restore ER to higher values post-initial decline. Conversely, our model demonstrates that entropy regularization mitigates this initial decrease in ER and gradually restores it to elevated levels over time.

The correlation between ground-truth and predicted entropy is depicted in Figure 8. The proposed methodology has a stronger correlation than that of the PU-Net, indicating better calibration. Furthermore the relationship between Effective rank and output entropy is inverse for both models. This indicates that mainly small variances dictate the variance of

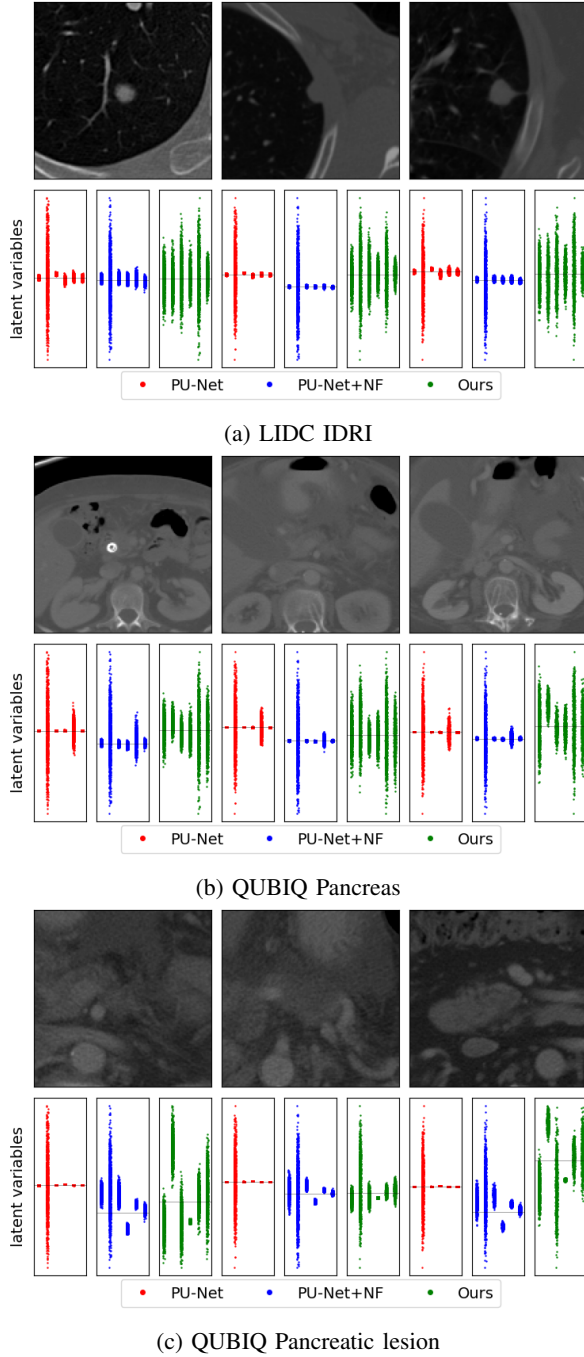


Fig. 4: Visualization of the latent vector mean and variances subject to various test images.

the predictions. This is a well-documented phenomenon in VAEs trained with fixed unitary-norm priors [60]. Notably, this behaviour is persistent when the prior is unconstrained.

Our experiments on latent sparsity include results on the PU-Net+NF and show that this model also decreases latent variance sparsity. Previous works argue that the augmentation of NFs results in a more complex and/or expressive posterior. Our results reveal that this method regularizes the relative condition numbers of the decoder by stretching the latent variances. In the context of the gradient descent, we can consider

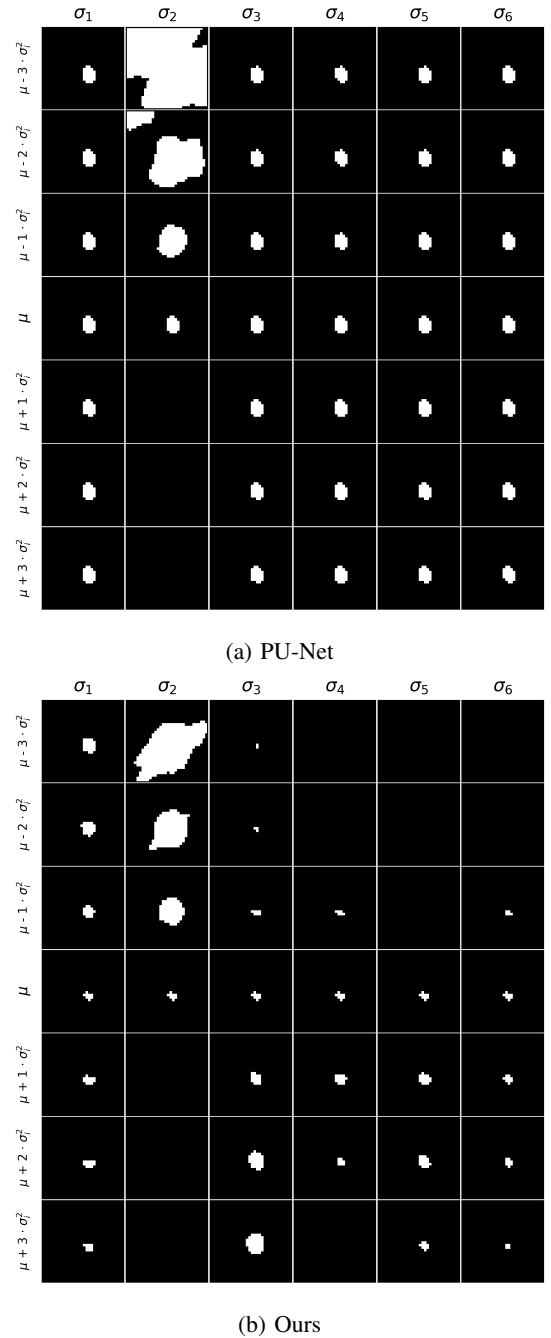


Fig. 5: Interpolation of the latent axis-aligned prior density for the LIDC-IDRI dataset (zoomed-in for viewing convenience).

augmenting with NFs as a form of preconditioning, where it smoothenes the optimization by an appropriate transformation on the latent samples. Nonetheless, the overall results indicate that this impact is marginal compared to the proposed SPU-Net.

To further demonstrate the general applicability of the proposed approach, we perform additional ablation experiments by replacing both the prior and posterior network with alternative convolutional encoders. In these experiments, we consider the ResNet [80] and ConvNext [81] architectures on the LIDC-IDRI dataset. Residual connections have shown to

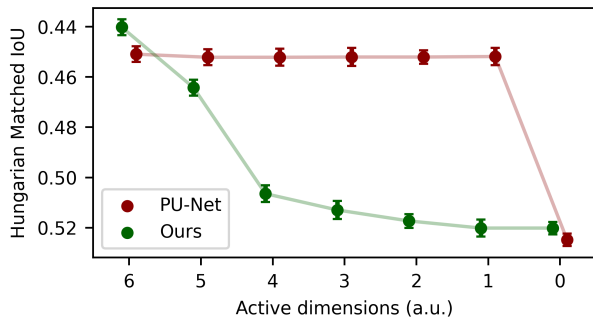
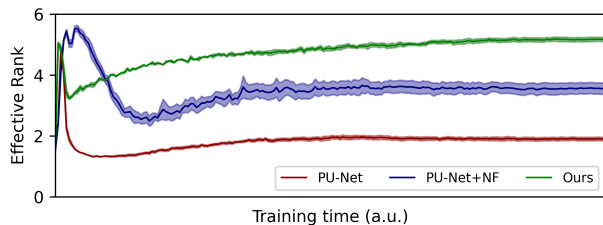
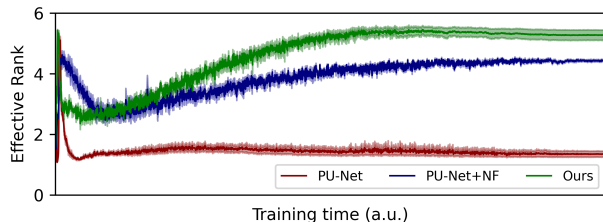


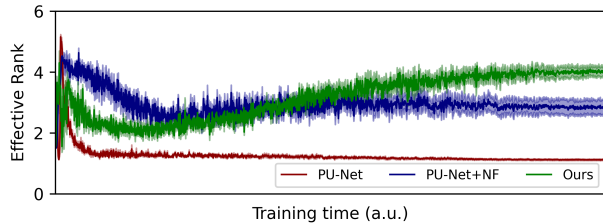
Fig. 6: Sequentially freezing latent dimensions (i.e. taking the mean) from smallest to largest. As can be seen the PU-Net is for a majority of the latent dimensions unaffected, while our proposed method suffers already from a single frozen dimension. This implies that the PU-Net does not use the information in variance



(a) LIDC IDRI



(b) QUBIQ pancreas



(c) QUBIQ pancreatic-lesion

Fig. 7: The effective rank during training for the evaluated models.

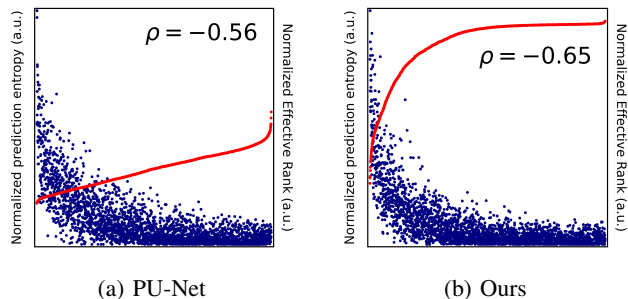


Fig. 8: Calibration between Effective Rank and prediction entropy for the LIDC-IDRI dataset, where ρ represents the Pearson correlation coefficient.

regulate problematic KL-divergences [24] and normalization mechanisms have also been employed in follow-up work on the PU-Net [26], [27]. The modified encoders are incorporated in the PU-Net and the results are presented in Table IV. While the baseline ResNet-based PU-Net does not exhibit any performance improvement, applying the proposed training strategy improved \hat{W}_k . Additionally, the ConvNext, introduced as an advancement over ResNet, demonstrates increased performance compared to ResNet in our experiments. Notably, \hat{W}_k further improves when the proposed training strategy is applied to the ConvNext-based PU-Net encoders.

Dataset	Model	$\hat{W}_k \downarrow$	ER \uparrow
LIDC-IDRI	ResNet	0.508	3.48
	ResNet (ours)	0.435	3.58
	ConvNext	0.451	1.47
	ConvNext (ours)	0.447	4.55

TABLE IV: Comparison of the PU-Net variants using different encoders with $d = 6$

V. LIMITATIONS

Despite the findings and insights in latent segmentation model behaviour, this research is subject to several limitations. Probabilistic segmentation metrics offer insight into the alignment between model predictions and ground-truth labels, but do not encapsulate the ultimate clinical objective, since the available labels merely serve as samples from the underlying distribution. Consequently, the evaluation metrics are valuable but are inherently limited as it only considers empirical samples from this distribution. As such, this approach is susceptible to overfitting on the available segmentation masks, rather than obtaining an appropriate estimation of the underlying ground-truth distribution. Therefore, a more comprehensive approach to evaluating probabilistic segmentation models involves the integration of domain expertise, which offers a nuanced understanding that transcends the limitations of quantitative metrics alone. Also, the U-Net used as a conditional decoder can be replaced with any architecture such as improved U-Net variants or transformers [82], [83]. This is beyond the scope of the paper and left for future work.

VI. CONCLUSION

In this work, we evaluate the Probabilistic U-Net on several multi-annotated datasets and have found that the performance is significantly inhibited due to the nature of the latent space. To alleviate this issue, we introduce a training scheme, which maximizes the mutual information in the Evidence Lower Bound and uses the entropy-regularized Sinkhorn Divergence in latent space. This approach encourages more informative and uniform latent space variances, improving probabilistic image segmentation for aleatoric uncertainty quantification in terms of the EWD metric. This research lays the groundwork for fostering an informative latent space in probabilistic segmentation models, and will be further explored through multi-resolution architectures, with the purpose of surpassing state-of-the-art performance. This research paves way for improved uncertainty quantification for image segmentation in the medical domain, thereby assisting clinicians with surgical planning and patient care.

REFERENCES

- [1] A. Kendall and Y. Gal, "What uncertainties do we need in bayesian deep learning for computer vision?," *NeurIPS*, vol. 30, 2017.
- [2] A. S. Becker, K. Chaitanya, K. Schawkat, U. J. Muehlemaier, A. M. Hötter, E. Konukoglu, and O. F. Donati, "Variability of manual segmentation of the prostate in axial t2-weighted mri: A multi-reader study," *European Journal of Radiology*, vol. 121, p. 108716, 2019.
- [3] B. H. Menze *et al.*, "The multimodal brain tumor image segmentation benchmark (brats)," *IEEE TMI*, vol. 34, no. 10, pp. 1993–2024, 2015.
- [4] A. Jungo, R. Meier, E. Ermis, M. Blatti-Moreno, E. Herrmann, R. Wiest, and M. Reyes, "On the effect of inter-observer variability for a reliable estimation of uncertainty of medical image segmentation," in *MICCAI*, pp. 682–690, Springer, 2018.
- [5] S. K. Warfield, K. H. Zou, and W. M. Wells, "Simultaneous truth and performance level estimation (staple): an algorithm for the validation of image segmentation," *IEEE TMI*, vol. 23, no. 7, pp. 903–921, 2004.
- [6] S. Vadineanu, D. Pelt, O. Dzyubachyk, and J. Batenburg, "An analysis of the impact of annotation errors on the accuracy of deep learning for cell segmentation," in *Medical Imaging with Deep Learning*, 2021.
- [7] F. van der Sommen, S. Zinger, E. J. Schoon, *et al.*, "Sweet-spot training for early esophageal cancer detection," in *Medical Imaging 2016: Computer-Aided Diagnosis*, vol. 9785, pp. 330–336, SPIE, 2016.
- [8] J. van der Putten, F. van der Sommen, J. de Groof, M. Struyvenberg, S. Zinger, W. Curvers, E. Schoon, J. Bergman, *et al.*, "Modeling clinical assessor intervariability using deep hypersphere encoder-decoder networks," *Neural Computing and Applications*, vol. 32, no. 14, pp. 10705–10717, 2020.
- [9] T. G. Boers, C. H. Kusters, K. N. Fockens, J. B. Jukema, M. R. Jong, J. de Groof, J. J. Bergman, F. van der Sommen, and P. H. de Wit, "Comparing training strategies using multi-assessor segmentation labels for barrett's neoplasia detection," in *CaPTion 2022, Held in Conjunction with MICCAI, Proceedings*, pp. 131–138, 2022.
- [10] L. Joskowicz, D. Cohen, N. Caplan, and J. Sosna, "Inter-observer variability of manual contour delineation of structures in ct," *European radiology*, vol. 29, no. 3, pp. 1391–1399, 2019.
- [11] T. Watadani, F. Sakai, T. Johkoh, S. Noma, M. Akira, K. Fujimoto, A. A. Bankier, K. S. Lee, N. L. Müller, J.-W. Song, *et al.*, "Interobserver variability in the ct assessment of honeycombing in the lungs," *Radiology*, vol. 266, no. 3, pp. 936–944, 2013.
- [12] E. Versteijne, O. J. Gurney-Champion, A. van der Horst, E. Lens, M. W. Kolff, J. Buijssen, G. Ebrahimi, K. J. Neelis, C. R. N. Rasch, J. Stoker, M. B. van Herk, A. Bel, and G. van Tienhoven, "Considerable interobserver variation in delineation of pancreatic cancer on 3dct and 4dct: a multi-institutional study," *Radiation Oncology (London, England)*, vol. 12, 2017.
- [13] I. Joo, J. M. Lee, E. S. Lee, J. Y. Son, D. H. Lee, S. J. Ahn, W. Chang, S. M. Lee, H.-J. Kang, and H. K. Yang, "Preoperative ct classification of the resectability of pancreatic cancer: Interobserver agreement," *Radiology*, p. 190422, 2019.
- [14] C. Viviers, M. Ramaekers, A. Valiuddin, T. Hellström, N. Tasios, J. van der Ven, I. Jacobs, L. Ewals, J. Nederend, M. Luyer, *et al.*, "Segmentation-based assessment of tumor-vessel involvement for surgical resectability prediction of pancreatic ductal adenocarcinoma," in *Proceedings of the IEEE/CVF International Conference on Computer Vision*, pp. 2421–2431, 2023.
- [15] A. Kendall, V. Badrinarayanan, and R. Cipolla, "Bayesian segnet: Model uncertainty in deep convolutional encoder-decoder architectures for scene understanding," *arXiv preprint arXiv:1511.02680*, 2015.
- [16] I. Osband, C. Blundell, A. Pritzel, and B. Van Roy, "Deep exploration via bootstrapped dqn," *NeurIPS*, vol. 29, 2016.
- [17] B. Lakshminarayanan, A. Pritzel, and C. Blundell, "Simple and scalable predictive uncertainty estimation using deep ensembles," *NeurIPS*, vol. 30, 2017.
- [18] C. Rupprecht, I. Laina, R. DiPietro, M. Baust, F. Tombari, N. Navab, and G. D. Hager, "Learning in an uncertain world: Representing ambiguity through multiple hypotheses," in *Proceedings of the ICCV*, pp. 3591–3600, 2017.
- [19] E. Ilg, O. Cicek, S. Galesso, A. Klein, O. Makansi, F. Hutter, and T. Brox, "Uncertainty estimates and multi-hypotheses networks for optical flow," in *Proceedings of the European Conference on Computer Vision (ECCV)*, pp. 652–667, 2018.
- [20] D. P. Kingma and M. Welling, "Auto-encoding variational bayes," *arXiv preprint arXiv:1312.6114*, 2013.
- [21] K. Sohn, H. Lee, and X. Yan, "Learning structured output representation using deep conditional generative models," in *NeurIPS*, vol. 28, Curran Associates, Inc., 2015.
- [22] O. Ronneberger, P. Fischer, and T. Brox, "U-net: Convolutional networks for biomedical image segmentation," in *MICCAI*, pp. 234–241, Springer, 2015.
- [23] C. F. Baumgartner, K. C. Tezcan, K. Chaitanya, A. M. Hötter, U. J. Muehlemaier, K. Schawkat, A. S. Becker, O. Donati, and E. Konukoglu, "Phiseg: Capturing uncertainty in medical image segmentation," in *MICCAI*, pp. 119–127, Springer, 2019.
- [24] S. A. Kohl, B. Romera-Paredes, K. H. Maier-Hein, D. J. Rezende, S. Eslami, P. Kohli, A. Zisserman, and O. Ronneberger, "A hierarchical probabilistic u-net for modeling multi-scale ambiguities," *arXiv preprint arXiv:1905.13077*, 2019.
- [25] E. Kassapis, G. Dikov, D. K. Gupta, and C. Nugteren, "Calibrated adversarial refinement for stochastic semantic segmentation," in *Proceedings of the IEEE/CVF International Conference on Computer Vision*, pp. 7057–7067, 2021.
- [26] M. Valiuddin, C. G. Viviers, R. J. van Sloun, F. v. d. Sommen, *et al.*, "Improving aleatoric uncertainty quantification in multi-annotated medical image segmentation with normalizing flows," in *UNSURE 2021, Held in Conjunction with MICCAI, Proceedings*, pp. 75–88, Springer, 2021.
- [27] R. Selvan, F. Faye, J. Middleton, and A. Pai, "Uncertainty quantification in medical image segmentation with normalizing flows," in *International Workshop on Machine Learning in Medical Imaging*, pp. 80–90, Springer, 2020.
- [28] I. Bhat, J. P. Pluim, M. A. Viergever, and H. J. Kuijff, "Effect of latent space distribution on the segmentation of images with multiple annotations," *arXiv preprint arXiv:2304.13476*, 2023.
- [29] K. Doi, H. MacMahon, S. Katsuragawa, R. M. Nishikawa, and Y. Jiang, "Computer-aided diagnosis in radiology: potential and pitfalls," *European journal of Radiology*, vol. 31, no. 2, pp. 97–109, 1999.
- [30] A. B. Rosenkrantz, R. P. Lim, M. Haghghi, M. B. Somberg, J. S. Babb, and S. S. Taneja, "Comparison of interreader reproducibility of the prostate imaging reporting and data system and likert scales for evaluation of multiparametric prostate mri," *American journal of roentgenology*, vol. 201, no. 4, pp. W612–W618, 2013.
- [31] M. Schaekermann, G. Beaton, M. Habib, A. Lim, K. Larson, and E. Law, "Understanding expert disagreement in medical data analysis through structured adjudication," *Proceedings of the ACM on Human-Computer Interaction*, vol. 3, no. CSCW, pp. 1–23, 2019.
- [32] A. S. Becker, K. Chaitanya, K. Schawkat, U. J. Muehlemaier, A. M. Hötter, E. Konukoglu, and O. F. Donati, "Variability of manual segmentation of the prostate in axial t2-weighted mri: a multi-reader study," *European journal of radiology*, vol. 121, p. 108716, 2019.
- [33] H. Fu, F. Li, Y. Xu, J. Liao, J. Xiong, J. Shen, J. Liu, X. Zhang, iChallenge-GON study group, *et al.*, "A retrospective comparison of deep learning to manual annotations for optic disc and optic cup segmentation in fundus photographs," *Translational vision science & technology*, vol. 9, no. 2, pp. 33–33, 2020.
- [34] L. Zbinden, L. Doorenbos, T. Pissas, R. Sznitman, and P. Márquez-Neila, "Stochastic segmentation with conditional categorical diffusion models," *arXiv preprint arXiv:2303.08888*, 2023.
- [35] T. Chen, R. Zhang, and G. Hinton, "Analog bits: Generating discrete data using diffusion models with self-conditioning," *arXiv preprint arXiv:2208.04202*, 2022.
- [36] A. Rahman, J. M. J. Valanarasu, I. Hacıhaliloglu, and V. M. Patel, "Ambiguous medical image segmentation using diffusion models," in *Proceedings of the IEEE/CVF Conference on Computer Vision and Pattern Recognition*, pp. 11536–11546, 2023.
- [37] S. Lee, B. Kim, and J. C. Ye, "Minimizing trajectory curvature of ode-based generative models," *arXiv preprint arXiv:2301.12003*, 2023.
- [38] J. Song, C. Meng, and S. Ermon, "Denosing diffusion implicit models," *arXiv preprint arXiv:2010.02502*, 2020.
- [39] M. Monteiro, L. Le Folgoc, D. Coelho de Castro, N. Pawlowski, B. Marques, K. Kamnitsas, M. van der Wilk, and B. Glocker, "Stochastic segmentation networks: Modelling spatially correlated aleatoric uncertainty," *Advances in neural information processing systems*, vol. 33, pp. 12756–12767, 2020.
- [40] S. Kohl, B. Romera-Paredes, C. Meyer, J. De Fauw, J. R. Ledsam, K. Maier-Hein, S. Eslami, D. Jimenez Rezende, and O. Ronneberger, "A probabilistic u-net for segmentation of ambiguous images," *NeurIPS*, vol. 31, 2018.
- [41] G. Wang, W. Li, M. Aertsen, J. Deprest, S. Ourselin, and T. Vercauteren, "Aleatoric uncertainty estimation with test-time augmentation for medical image segmentation with convolutional neural networks," *Neurocomputing*, vol. 338, pp. 34–45, 2019.
- [42] W. Ji, S. Yu, J. Wu, K. Ma, C. Bian, Q. Bi, J. Li, H. Liu, L. Cheng, and Y. Zheng, "Learning calibrated medical image segmentation via multi-

- ater agreement modeling,” in *Proceedings of the IEEE/CVF Conference on Computer Vision and Pattern Recognition*, pp. 12341–12351, 2021.
- [43] X. Guo, S. Lu, Y. Yang, P. Shi, C. Ye, Y. Xiang, and T. Ma, “Modeling annotator variation and annotator preference for multiple annotations medical image segmentation,” *2022 IEEE International Conference on Bioinformatics and Biomedicine (BIBM)*, pp. 977–984, 2022.
- [44] C. G. Viviers, M. A. Valiuddin, F. van der Sommen, et al., “Probabilistic 3d segmentation for aleatoric uncertainty quantification in full 3d medical data,” in *Medical Imaging 2023: Computer-Aided Diagnosis*, vol. 12465, pp. 341–351, SPIE, 2023.
- [45] I. Bhat, J. P. Plum, and H. J. Kuijf, “Generalized probabilistic u-net for medical image segmentation,” in *UNSURE 2022, Held in Conjunction with MICCAI, Proceedings*, pp. 113–124, Springer, 2022.
- [46] S. Zhao, J. Song, and S. Ermon, “Infovae: Information maximizing variational autoencoders,” *arXiv preprint arXiv:1706.02262*, 2017.
- [47] C. Cremer, X. Li, and D. Duvenaud, “Inference suboptimality in variational autoencoders,” in *ICML*, pp. 1078–1086, PMLR, 2018.
- [48] Y. Zheng, T. He, Y. Qiu, and D. P. Wipf, “Learning manifold dimensions with conditional variational autoencoders,” *Advances in Neural Information Processing Systems*, vol. 35, pp. 34709–34721, 2022.
- [49] X. Chen, D. P. Kingma, T. Salimans, Y. Duan, P. Dhariwal, J. Schulman, I. Sutskever, and P. Abbeel, “Variational lossy autoencoder,” *arXiv preprint arXiv:1611.02731*, 2016.
- [50] S. R. Bowman, L. Vilnis, O. Vinyals, A. M. Dai, R. Jozefowicz, and S. Bengio, “Generating sentences from a continuous space,” *arXiv preprint arXiv:1511.06349*, 2015.
- [51] I. Serban, A. Sordoni, R. Lowe, L. Charlin, J. Pineau, A. Courville, and Y. Bengio, “A hierarchical latent variable encoder-decoder model for generating dialogues,” in *Proceedings of the AAAI conference on artificial intelligence*, vol. 31, 2017.
- [52] M. Fraccaro, S. K. Sønderby, U. Paquet, and O. Winther, “Sequential neural models with stochastic layers,” *Advances in neural information processing systems*, vol. 29, 2016.
- [53] N. V. Alger et al., *Data-scalable Hessian preconditioning for distributed parameter PDE-constrained inverse problems*. PhD thesis, 2019.
- [54] S. Ioffe and C. Szegedy, “Batch normalization: Accelerating deep network training by reducing internal covariate shift,” in *International conference on machine learning*, pp. 448–456, PMLR, 2015.
- [55] T. Salimans and D. P. Kingma, “Weight normalization: A simple reparameterization to accelerate training of deep neural networks,” *Advances in neural information processing systems*, vol. 29, 2016.
- [56] J. L. Ba, J. R. Kiros, and G. E. Hinton, “Layer normalization,” *arXiv preprint arXiv:1607.06450*, 2016.
- [57] Y. Wu and K. He, “Group normalization,” in *Proceedings of the European conference on computer vision (ECCV)*, pp. 3–19, 2018.
- [58] S. Qiao, H. Wang, C. Liu, W. Shen, and A. Yuille, “Micro-batch training with batch-channel normalization and weight standardization,” *arXiv preprint arXiv:1903.10520*, 2019.
- [59] D. Rezende and S. Mohamed, “Variational inference with normalizing flows,” in *ICML*, pp. 1530–1538, PMLR, 2015.
- [60] B. Dai and D. Wipf, “Diagnosing and enhancing vae models,” *arXiv preprint arXiv:1903.05789*, 2019.
- [61] C. Villani, *Optimal Transport: Old and New*. Springer Berlin Heidelberg, 2008.
- [62] A. Wilson, *The Use of Entropy Maximising Models in the Theory of Trip Distribution, Mode Split and Route Split*. Centre for Environmental Studies, 1968.
- [63] M. Cuturi, “Sinkhorn distances: Lightspeed computation of optimal transport,” *NeurIPS*, vol. 26, 2013.
- [64] A. Genevay, L. Chizat, F. Bach, M. Cuturi, and G. Peyré, “Sample complexity of sinkhorn divergences,” in *The 22nd International Conference on Artificial Intelligence and Statistics*, pp. 1574–1583, PMLR, 2019.
- [65] J. J. Kosowsky and A. L. Yuille, “The invisible hand algorithm: Solving the assignment problem with statistical physics,” *Neural networks*, vol. 7, no. 3, pp. 477–490, 1994.
- [66] O. Bousquet, S. Gelly, I. Tolstikhin, C.-J. Simon-Gabriel, and B. Schoelkopf, “From optimal transport to generative modeling: the vegan cookbook,” 2017.
- [67] I. Tolstikhin, O. Bousquet, S. Gelly, and B. Schoelkopf, “Wasserstein auto-encoders,” 2019.
- [68] L. N. Vaserstein, “Markov processes over denumerable products of spaces, describing large systems of automata,” *Problemy Peredachi Informatsii*, vol. 5, no. 3, pp. 64–72, 1969.
- [69] G. Patrini, R. van den Berg, P. Forre, M. Carioni, S. Bhargav, M. Welling, T. Genewein, and F. Nielsen, “Sinkhorn autoencoders,” in *Uncertainty in Artificial Intelligence*, pp. 733–743, PMLR, 2020.
- [70] I. Higgins, L. Matthey, A. Pal, C. P. Burgess, X. Glorot, M. M. Botvinick, S. Mohamed, and A. Lerchner, “beta-vae: Learning basic visual concepts with a constrained variational framework,” *ICLR (Poster)*, vol. 3, 2017.
- [71] J. Feydy, T. Séjourné, F.-X. Vialard, S.-i. Amari, A. Trounev, and G. Peyré, “Interpolating between optimal transport and mmd using sinkhorn divergences,” in *The 22nd International Conference on Artificial Intelligence and Statistics*, pp. 2681–2690, PMLR, 2019.
- [72] S. Armato III, G. McLennan, L. Bidaut, M. McNitt-Gray, C. Meyer, A. Reeves, B. Zhao, D. Aberle, C. Henschke, E. Hoffman, E. Kazerooni, H. Macmahon, E. Beek, D. Yankelevitz, A. Biancardi, P. Bland, M. Brown, R. Engelmann, G. Laderach, and L. Clarke, “The lung image database consortium (lidc) and image database resource initiative (idri): A completed reference database of lung nodules on ct scans,” *Medical Physics*, vol. 38, pp. 915–931, 01 2011.
- [73] B. Menze, L. Joskowicz, S. Bakas, A. Jakab, E. Konukoglu, A. Becker, A. Simpson, and R. Do, “Quantification of Uncertainties in Biomedical Image Quantification 2021,” Mar. 2021.
- [74] A. Schreuder, E. T. Scholten, B. van Ginneken, and C. Jacobs, “Artificial intelligence for detection and characterization of pulmonary nodules in lung cancer ct screening: ready for practice?,” *Translational lung cancer research*, vol. 10, no. 5, p. 2378, 2021.
- [75] F. Ciompi, K. Chung, S. J. Van Riel, A. A. A. Setio, P. K. Gerke, C. Jacobs, E. T. Scholten, C. Schaefer-Prokop, M. M. Wille, A. Marchiano, et al., “Towards automatic pulmonary nodule management in lung cancer screening with deep learning,” *Scientific reports*, vol. 7, no. 1, p. 46479, 2017.
- [76] S. Lam and M. Tammemagi, “Contemporary issues in the implementation of lung cancer screening,” *European Respiratory Review*, vol. 30, no. 161, 2021.
- [77] G. P. LeMense, E. A. Waller, C. Campbell, and T. Bowen, “Development and outcomes of a comprehensive multidisciplinary incidental lung nodule and lung cancer screening program,” *BMC pulmonary medicine*, vol. 20, pp. 1–8, 2020.
- [78] A. R. Jazieh, M. AlGhamdi, S. AlGhanem, M. AlGarni, K. AlKattan, M. AlRujaib, M. AlNaimi, O. M. Babelli, S. AlShehri, R. AlQahtani, et al., “Saudi lung cancer prevention and screening guidelines,” *Annals of Thoracic Medicine*, vol. 13, no. 4, p. 198, 2018.
- [79] O. Roy and M. Vetterli, “The effective rank: A measure of effective dimensionality,” in *2007 15th European signal processing conference*, pp. 606–610, IEEE, 2007.
- [80] K. He, X. Zhang, S. Ren, and J. Sun, “Deep residual learning for image recognition,” in *Proceedings of the IEEE conference on computer vision and pattern recognition*, pp. 770–778, 2016.
- [81] Z. Liu, H. Mao, C.-Y. Wu, C. Feichtenhofer, T. Darrell, and S. Xie, “A convnet for the 2020s,” in *Proceedings of the IEEE/CVF conference on computer vision and pattern recognition*, pp. 11976–11986, 2022.
- [82] J. Chen, Y. Lu, Q. Yu, X. Luo, E. Adeli, Y. Wang, L. Lu, A. L. Yuille, and Y. Zhou, “Transunet: Transformers make strong encoders for medical image segmentation,” *arXiv preprint arXiv:2102.04306*, 2021.
- [83] A. Dosovitskiy, L. Beyer, A. Kolesnikov, D. Weissenborn, X. Zhai, T. Unterthiner, M. Dehghani, M. Minderer, G. Heigold, S. Gelly, J. Uszkoreit, and N. Houlsby, “An image is worth 16x16 words: Transformers for image recognition at scale,” *CoRR*, vol. abs/2010.11929, 2020.